The Journal of Chemical Physics ARTICLE scitation.org/journal/jcp

A variable time step self-consistent mean field DSMC model for three-dimensional environments

Cite as: J. Chem. Phys. 156, 124309 (2022); doi: 10.1063/5.0083033
Submitted: 21 December 2021 • Accepted: 7 March 2022 •
Published Online: 31 March 2022

O. Schullian,[1,2] H. S. Antila,[1,3] and B. R. Heazlewood[4,a)]

AFFILIATIONS

[1] Department of Theory and Bio-Systems, Max Planck Institute of Colloids and Interfaces, Potsdam-Golm Science Park, 14476 Potsdam, Germany
[2] Fachbereich Physik, Freie Universität Berlin, 14195 Berlin, Germany
[3] Department of Biomaterials, Max Planck Institute of Colloids and Interfaces, Potsdam-Golm Science Park, 14476 Potsdam, Germany
[4] Department of Physics, University of Liverpool, Liverpool L69 7ZE, United Kingdom

[a)] **Author to whom correspondence should be addressed:** b.r.heazlewood@liverpool.ac.uk

ABSTRACT

A self-consistent mean field direct simulation Monte Carlo (SCMFD) algorithm was recently proposed for simulating collision environments for a range of one-dimensional model systems. This work extends the one-dimensional SCMFD approach to three dimensions and introduces a variable time step (3D-vt-SCMFD), enabling the modeling of a considerably wider range of different collision environments. We demonstrate the performance of the augmented method by modeling a varied set of test systems: ideal gas mixtures, Poiseuille flow of argon, and expansion of gas into high vacuum. For the gas mixtures, the 3D-vt-SCMFD method reproduces the properties (mean free path, mean free time, collision frequency, and temperature) in excellent agreement with theoretical predictions. From the Poiseuille flow simulations, we extract flow profiles that agree with the solution to the Navier–Stokes equations in the high-density limit and resemble free molecular flow at low densities, as expected. The measured viscosity from 3D-vt-SCMF is ~15% lower than the theoretical prediction from Chapman–Enskog theory. The expansion of gas into vacuum is examined in the effusive regime and at the hydrodynamic limit. In both cases, 3D-vt-SCMDF simulations produce gas beam density, velocity, and temperature profiles in excellent agreement with analytical models. In summary, our tests show that 3D-vt-SCMFD is robust and computationally efficient, while also illustrating the diversity of systems the SCMFD model can be successfully applied to.

I. INTRODUCTION

Despite the variety of multi- and mesoscale simulation methods developed over the past several decades,[1–8] some typical gas-phase environments are still challenging to model. This is the case, for example, when the species of interest is a trace component present in a mixture—a situation typical for buffer gas cell environments,[9,10] expansions of gas mixtures through a valve,[11] and atomic layer deposition.[12] Therein, the requirement that simulated particles represent the relative numbers and types of physical particles can be onerous for models using particle-based methods.

Of particular interest to us are buffer gas cell environments. Recent years have seen considerable experimental advances in the use of buffer gas cells to collisionally cool molecular species of interest. Unlike methods that employ external fields—which typically require the molecules of interest to exhibit a closed laser cooling cycle, possess a permanent electric dipole, or be paramagnetic—buffer gas cooling can be applied to a broad range of molecular species.[13,14] It is practically challenging to experimentally probe the conditions within the cell itself, as buffer gas cells are typically small (with dimensions on the order of a few cm^3) enclosed spaces. While the properties of the species that successfully exit the cell can be established, such measurements do not reveal how the collisions occurred in the cell. (For example, if molecules undergo sufficient collisions to reach the desired final temperature within the first few mm of a 2 cm-long cell,

a much smaller cell could be used.) As such, simulations perform an important role in guiding the design and optimization of buffer gas cells, in addition to revealing the details of the collision properties.

One method that has been successfully used to simulate buffer gas cells[15,16] is the direct simulation Monte Carlo (DSMC) method developed by Bird in the 1960s.[1,2] The central concept of DSMC is that, instead of simulating all particles, the behavior of the system of interest can be accurately reproduced by modeling only a fraction of the physical particles. Each of the small number of "simulated" particles represents a large number of physical particles, given by the factor f_n. The simulated particles are propagated through the system, which is overlaid with a grid of subcells whose size must be smaller than the mean free path as well as the characteristic length scales of the system (e.g., a valve opening). Each iteration is separated into two steps: (1) ballistic propagation, where each particle is propagated for a time step without taking other particles into account, and (2) collision, where the particles can collide with other particles in the same subcell in a stochastic manner based on their pairwise collision probabilities. The DSMC method is particularly powerful owing to the impressive range of length and time scales available, ranging from meso to macro, and it has been successfully applied to a wide variety of systems in field spanning from aeronautics (modeling gas flows for a spacecraft)[17] to materials processing (describing thin film growth and plasma etching).[18] DSMC is also able to describe non-equilibrium systems, whereas many of the alternatives, such as the Lattice–Boltzmann method,[5,6] may struggle to do so.[19]

Despite the impressive range of applications, DSMC simulations for systems with trace components are still inefficient and costly (in some cases even impossible) to implement—owing to the large number of particles needed to replicate the range of concentrations present and accurately extract the collision properties. Several variations of the DSMC method have been previously introduced in an attempt to model the collisions of trace species, including Bird's non-conservative weighting scheme[1] and the conservative weighting scheme of Boyd.[20] However, both these algorithms only conserve energy and momentum on average (and not exactly). While the stochastic weighted particle approach introduced by Rjasanow and Wagner[21] avoids energy and momentum conservation issues, it was developed for the modeling of monatomic gases—a much simpler system than the complex collision environments and gas mixtures of interest in this work. A hybrid approach based on DSMC was recently introduced for the simulation of cryogenic buffer gas cell environments. The first step modeled the background gas using a traditional DSMC approach. The second step involved a random walk through the background gas, with the properties of individual species of interest subsequently tracked (using a random collision model) as they travel through the buffer gas cell environment.[22] By combining the benefits of DSMC with particle tracing capabilities, the hybrid approach was found to successfully reproduce several experimentally measured properties of cryogenic buffer gas cell beams. The same concept was successfully used to model the reaction $H_2^+ + H_2 \rightarrow H_3^+ + H$ and measure the rate coefficients. Therein, the background gas was determined experimentally and the individual test particles were tracked through an expanding beam and subsequently detected using an electric ejection pulse.[23,24]

Similar to the hybrid method described above, the self-consistent mean field direct simulation Monte Carlo[25] (SCMFD) approach takes advantage of the benefits of DSMC while enabling particle tracking. In SCMFD, a mean field—used to describe the background gas environment—is constructed by considering the trajectories of a representative number of particles. A single particle does not influence the properties of the mean field; it is only one particle in an environment made up of trillions of particles. Therefore, once the mean field is constructed, the collisions of particles of interest can be explicitly traced as they travel through the mean field. Where collisions between the same types of particles occur, the properties of the mean field are updated. The key difference to the hybrid approach is that SCMFD makes the simulation feasible by lifting the requirement to replicate the physical ratio of different species, rather than by requiring two sets of simulations (i.e., both DSMC simulations and additional random collision particle-tracing simulations, as implemented in the hybrid method). Both the SCMFD and hybrid approaches appear to be valid methods for simulating collisions in buffer gas cell environments or other stationary flows, where the background gas (the mean field) is a steady-state (i.e., time-independent) environment. The key benefit of the SCMFD approach is the computational efficiency: SCMFD calculations require significantly less memory and time than DSMC calculations, without sacrificing accuracy.

Here, we have augmented the SCMFD method to consider three-dimensional (3D) gas-phase environments along with the use of a variable time step to boost the efficiency. The 3D-variable time step SCMFD (3D-vt-SCMFD) model is then applied to three different gas-phase systems to demonstrate its performance: gas mixtures, Poiseuille flows, and expansions from a high-pressure reservoir into a low-pressure region. In all three cases, 3D-vt-SCMFD successfully replicates the properties of the particles of interest, in excellent agreement with analytical models. These findings show the robustness and broad applicability of the 3D-vt-SCMFD method in modeling diverse gas-phase environments.

II. METHOD

The method devised for one-dimensional SCMFD simulations was described in detail in a previous publication.[25] The key steps are summarized here and can be seen in Fig. 1: First, an initial mean field density ρ_0, representing the background gas, is defined. A test particle is then flown through ρ_0, and the trajectory is used to calculate a density and velocity distribution $\tilde{\rho}$. To ensure sufficient sampling of $\tilde{\rho}$, the trajectory length is chosen such that the test particle undergoes several thousand collisions with the walls. Subsequently, the mean field density ρ_0 is updated according to the expression

$$\rho_0(\mathbf{x},\mathbf{v}) = (1-r)\rho_0(\mathbf{x},\mathbf{v}) + r\tilde{\rho}(\mathbf{x},\mathbf{v}), \tag{1}$$

where r is a parameter with $0 \le r \le 1$, used for more stability in convergence. The loop is repeated until the mean field density converges, which is reached when the average density, average velocity, average temperature, number of collisions per trajectory, mean

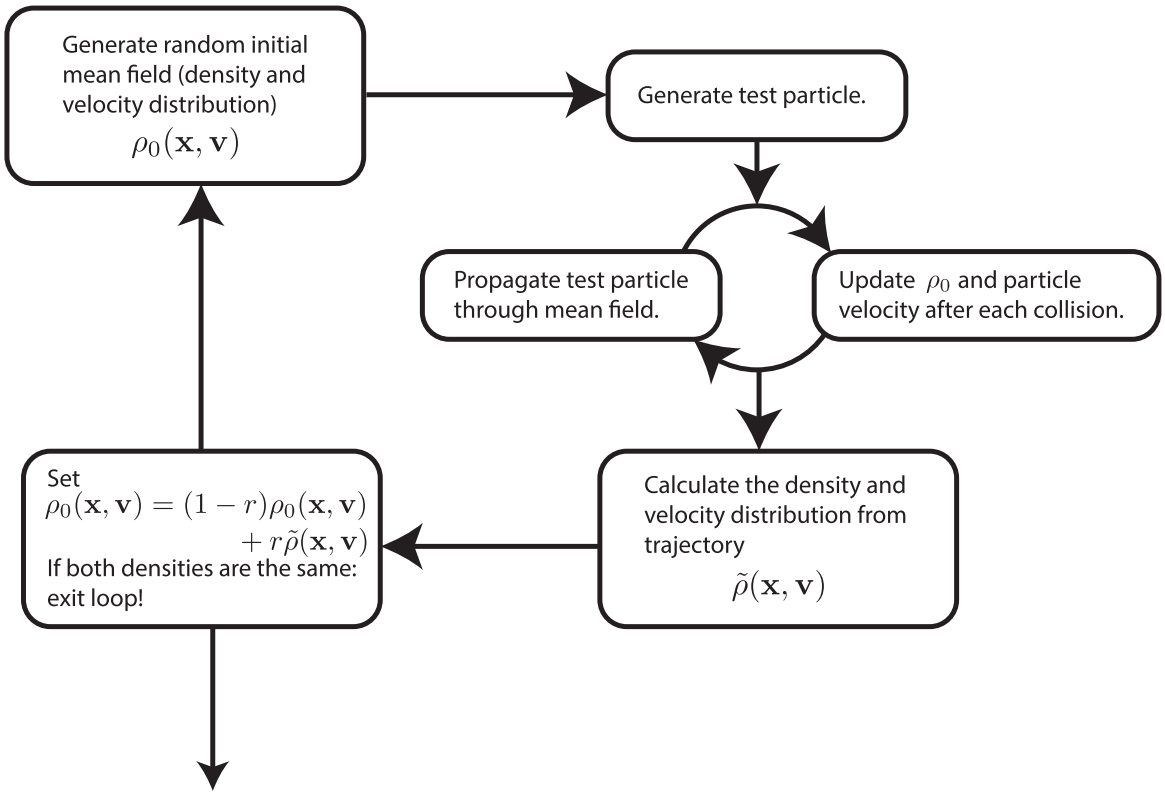

FIG. 1. Flowchart depicting the SCMFD algorithm.

free time, and mean free path are (approximately) constant from one iteration to the next. After initial convergence, data collection on the simulated system can be initiated. However, the background mean field is still periodically updated based on the recorded trajectory [$\tilde{\rho}$, according to Eq. (1)], in addition to local subcell mean field updates to ρ_0, which occur whenever the simulated particle interacts with the background gas (see below).

For the calculation of individual particle trajectories, a particle is generated with an initial position and velocity. The particle is then propagated through the mean field background gas for a time step of δt. If the particle has moved beyond the confines of the simulated volume, it is either reflected (diffusely or mirrored) from the boundary wall or eliminated from the simulation. The probability of the simulated particle colliding with the background gas is then calculated, as in the one-dimensional SCMFD model.[25] If no collision occurs, the process is repeated, and the particle is propagated for another time step. To reproduce the correct collision properties (such as collision frequency and mean free time), the time step must be much shorter than the mean free time, as in DSMC.[26] We have found that δt smaller than 1% of mean free time is required for most systems. Therefore, using a fixed time step can be inefficient, as in many cases, particles will be propagated for multiple time steps without undergoing a single collision. In the 3D-vt-SCMFD method, the number of time steps where no collisions occur is taken into account analytically, and the size of the time step is adjusted so that, whenever a particle is propagated, a collision occurs (see Sec. II A for derivation).

When the simulated particle undergoes a collision, the protocol for evaluating the outcome of a collision is adopted following the approach detailed in previous work:[25] The collisions are treated as elastic, binary, hard-sphere collisions. Energy and momentum conservation require that only the direction of the relative velocity of the collision partners, but not its magnitude, can change. The final direction is fully defined by the impact parameter—which in SCMFD is uniformly distributed on a disk, leading to a distribution of the final direction of the relative velocity that is uniform on a sphere. It is important to note that the formation of a mean field and the treatment of collisions within SCMFD are different from the approach proposed by Nanbu in an earlier variation of the conventional DSMC method, introduced in 1980.[27] A key limitation of Nanbu's method was the lack of momentum and energy conservation,[28] with only the velocity of one collision partner updated following a collision. In contrast, the SCMFD method adopts an identical approach to momentum and energy conservation as is implemented in the conventional DSMC method—with this approach thoroughly tested and validated over the past several decades.

The properties of the background gas—the mean field—within a collision cell are updated *only* when the particle being propagated collides with another particle of the same species. As previously

noted,[25] this improves the convergence properties and enables us to exclusively track the species of interest. Adjusting the properties of the mean field following every collision (including collisions between different species) would necessitate replicating the physical ratio of all species in the mixture in the simulations; else, the frequency of energy exchange between the species of interest and the background gas would be overestimated.

The key benefits of the 3D-vt-SCMFD approach can be summarized as follows:

1. There is no need to convert between simulated particles and physical particles.
2. As individual particles can be tracked, there is no need to explicitly reproduce the same relative numbers of each type of species in the physical system of interest. This is particularly relevant for systems where the species of interest is a minor component of the gas mixture as for these systems, traditional DSMC models (where all particles typically need to be propagated simultaneously) can become unfeasible. Once the mean field has been generated, the SCMFD approach allows resources to be focused exclusively on the species of interest.
3. When a collision does not occur at a given time step, the collision probability does not change. This enables the use of a variable-size time step, which can be adjusted on-the-fly by considering the free time between collisions in a selected region. The introduction of a variable time step makes the code far more efficient without sacrificing accuracy.

A. Variable time step based on expected free time between collisions

For the one-dimensional SCMFD, we opted for a simple implementation with a fixed simulation time step. The potential computational gain associated with using a variable time step becomes more attractive with increasing system size and dimensionality, which motivated us to incorporate this upgrade into the 3D-vt-SCMFD method. The optimal size of the time step depends on the properties of the system: it must be several orders of magnitude smaller than the average mean free time between collisions to retain accuracy. In systems containing a range of different densities, the magnitude of the fixed time step is determined by the region of highest density—the highest collision frequency. However, an unnecessarily high number of time steps are then calculated in low-density regions. Using a variable time step allows for on-the-fly adaptation to the surrounding system properties, achieving a computationally efficient simulation without compromising on the precision. Previous approaches have sought to improve the efficiency of DSMC calculations by varying the length of the time step (as initially implemented in Bird's time counter scheme) or by considering only a fraction of all possible collision partners at a given time step (as in the no-time-counter method).[29] Takahashi *et al.* altered the time step "dynamically" in their hybrid DSMC method, to maintain a constant collision probability.[22] As we track single particles traveling through the mean field, we cannot choose to consider fewer collision partners. Instead, we establish when the next collision with the trace particle will occur by calculating the free time between collisions directly. By side-stepping the use of random numbers in combination with collision probabilities to determine collision events, the efficiency of the SCMFD algorithm is significantly improved.

The probability that no collisions occur in a subcell in a selected time interval can be defined as[25]

$$P_{nc} = e^{-\delta t \langle v_r \sigma \rangle \rho}. \tag{2}$$

A small time interval, δt, and appropriate subcell dimensions are selected such that the term $\langle v_r \sigma \rangle$, where v_r is the relative velocity and σ is the collision cross section, does not change during the time interval. The density of the subcell is defined as ρ. The probability of at least one collision occurring during time step δt is then given by $P_c = 1 - P_{nc}$. Due to the Markovian property of the collision dynamics, Eq. (2) is valid for all values of δt (as is the expression for P_c). We can subsequently define the probability of at least one collision occurring in the time interval $[0, t_2]$ as the sum of the probability of at least one collision occurring between $[0, t_1]$ and the probability of one or more collisions occurring in the interval $[t_1, t_2]$ with no collision between $[0, t_1]$,

$$P_{[0,t_1]} + P_{[t_1,t_2]|\text{no collisions in } [0,t_1]} = P_{[0,t_2]}. \tag{3}$$

For the interval $[t_1, t_2]$, the conditional collision probability (where no collision occurs before t_1) follows by the rearrangement of Eq. (3),

$$\begin{aligned} P_{[t_1,t_2]|\text{no collisions in } [0,t_1]} &= P_{[0,t_2]} - P_{[0,t_1]} \\ &= 1 - e^{-\langle v_r \sigma \rangle \rho t_2} - 1 + e^{-\langle v_r \sigma \rangle \rho t_1} \\ &= -e^{-t \langle v_r \sigma \rangle \rho} \Big|_{t=t_1}^{t_2} \\ &= \int_{t_1}^{t_2} \mathrm{d}t e^{-t \langle v_r \sigma \rangle \rho} \langle v_r \sigma \rangle \rho, \end{aligned} \tag{4}$$

yielding a normalized density distribution function for the (collision) free time t. The corresponding cumulative distribution function is given by

$$\begin{aligned} cdf(t) &= -e^{-t' \langle v_r \sigma \rangle \rho} \Big|_{t'=0}^{t} \\ &= -e^{-t \langle v_r \sigma \rangle \rho} + e^{-0 \langle v_r \sigma \rangle \rho} \\ &= 1 - e^{-t \langle v_r \sigma \rangle \rho}. \end{aligned} \tag{5}$$

Generating a uniformly distributed random number $\alpha \in [0, 1)$ and inverting the expression, we obtain an expression

$$t_\alpha = -\frac{\log(1-\alpha)}{\langle v_r \sigma \rangle \rho} \tag{6}$$

for calculating the free time between collisions, t_r, representing the time step over which a particle needs to be propagated until the next collision occurs. For mixtures of different gaseous species, the free time between collisions can be written as

$$t_\alpha^j = -\frac{\log(1-\alpha)}{\sum_{i=1}^{n_p} \langle v_{ji}^r \sigma_{ji} \rangle \rho_i}, \tag{7}$$

where j is the index of the species of interest, from a total of n_p different species.

B. Special considerations for 3D-vt-SCMFD

When switching from one-dimensional to three-dimensional systems, it is necessary to consider the presence of corners and edges, which can lead to a particle crossing multiple boundaries within a single time step, increasing the complexity of the problem. The challenge of identifying the first boundary that a particle trajectory crosses can be circumvented with the use of a variable time step.

At every stage of the simulation, four different times are considered: t_r, given by Eq. (6), and the time for the particle to move (for each of the x, y, and z directions) into the next subcell. For example, if the particle is in subcell n_x at position x and has positive velocity v_x in the x direction, the time taken for it to move into the subcell $n_x + 1$ along the x axis is given by $\delta t_x = (n_x L_x/n_{\text{cell,x}} - x)/v_x$, where L_x is the length of the simulation box and $n_{\text{cell,x}}$ is the number of subcells in the x direction [for negative velocity, the time is given by $\delta t_x = ((n_x - 1)L_x/n_{\text{cell,x}} - x)/v_x$]. The method then chooses the smallest of these four values (identifying the smallest time step that leads to a collision or movement into a different subcell) and propagates the particle for that time step. In the case of an accelerated flow, such as the pressure-driven Poiseuille flow, the method includes a fifth value, $\Delta t_{\max}$ (a simulation input), which sets an upper limit for the change in the velocity during a time step ($\Delta v = a\Delta t_{\max}$, where a is the acceleration).

Depending on which time is the smallest, the method performs different routines: If t_r [from Eq. (6)] is the smallest, then a collision occurs; if the smallest time step is $\Delta t_{\max}$, the particle is propagated and nothing happens. In the three other cases, the particle has moved from one subcell to another (it is located at the boundary of the next subcell). However, if that next subcell does not exist—if the next subcell is outside the simulation—then the particle is deemed to be at the location of the simulation boundary. Based on the type of boundary, a thermal, periodic, or mirrored reflection is performed and the velocity is readjusted; otherwise, the particle is eliminated from the simulation.

III. RESULTS AND DISCUSSION

To demonstrate the accuracy and applicability of the 3D-vt-SCMFD approach, we model three well-characterized gas-phase environments: (A) a gas mixture with one component present as a (trace) seed gas, (B) a gaseous Poiseuille flow at a range of densities, and (C) a gas expansion from a high pressure region into vacuum. Each of these scenarios is discussed below, accompanied by a detailed comparison of the simulation results with previous work and theoretical predictions.

A. Gas mixtures

First, we use 3D-vt-SCMFD to simulate an ideal gas mixture in three dimensions. A gas mixture is described as ideal when individual gas particles can be modeled as hard spheres with no internal degrees of freedom (not to be confused with an ideal gas where the particles have no volume). The key benefit of simulating an ideal gas mixture is the ability to benchmark the findings of the 3D-vt-SCMFD method against quantities that can be calculated analytically.

TABLE I. Comparison of the temperature (in K) between the 3D-vt-SCMFD predictions and wall temperature of 273 K for collisions in a box of 1 cm^3 volume.

Parameter	Ar	He	N_2
T_x	272.990 ± 0.019	273.003 ± 0.008	273.021 ± 0.018
T_y	273.014 ± 0.018	272.991 ± 0.011	273.021 ± 0.019
T_z	273.002 ± 0.006	273.010 ± 0.010	273.006 ± 0.013

We simulate a three-component gas mixture where each of the particles are hard spheres, with parameters (mass and diameter) chosen so that they represent Ar, He, and N_2. The gases are present at concentrations spanning six orders of magnitude with number densities of 10^{20} m^{-3} (Ar), 10^{18} m^{-3} (He), and 10^{14} m^{-3} (N_2). The gas mixture is contained within a constant-volume, cube-shaped box with sides of 1 cm length, enclosed by thermal walls (at a temperature of 273 K) that act as a thermostat. All other particle and simulation parameters are defined in Table S2 of the supplementary material.

First, the temperature of each particle type is calculated from the sampled velocities using $T_i = \frac{m}{k_B}\langle(v_i - \langle v_i\rangle)^2\rangle$, where m is the mass of the respective particle type and v_i is the velocity in one dimension with $i = x, y, z$. The simulated temperatures, shown in Table I, correspond well to the temperature of the wall (at 273 K). Two temperatures (out of nine) are outside one standard error of mean (SEOM); they are still within 1.12 SEOM and 1.17 SEOM, respectively.

We then proceed to quantify the mean free path, mean free time between collisions (Table II), and the collision frequency (Table III) from the simulation. The values are in excellent agreement with those obtained analytically [Eqs. (8)–(11) in Ref. 25 or see Ref. 1 for the derivation], for all collision types (Ar–Ar, Ar–He, Ar–N_2, He–He, He–N_2, and N_2–N_2).

The concentration of N_2 in the test system is chosen to be 6 orders of magnitude smaller than that of Ar to demonstrate key advantage of the SCMFD approach—the ability to efficiently model systems with a wide range of concentrations, such as those where the species of interest is a trace component. Conversely, simulating the system using DSMC is highly time consuming because it would require a minimum amount (≥100) of N_2 particles and consequently $\geq 10^8$ Ar particles.

B. Poiseuille flow

In this subsection, we probe the ability of 3D-vt-SCMFD to model a gaseous Poiseuille flow—a pressure-driven flow through a channel with (partial) slip boundary conditions that forms a parabolic flow profile. As in Subsection III A, the Poiseuille flow is selected as a test system for 3D-vt-SCMFD as it allows the findings to be compared with those calculated from well-established methods. In this case, however, these established methods are known to have limitations; they can only describe the flow under certain conditions. Hence, we also probe the ability of 3D-vt-SCMFD to accurately model Poiseuille flows over a wide range of densities.

TABLE II. Comparison of the mean free path (in m) and mean free time (in s) between the 3D-vt-SCMFD predictions and analytical values [Eqs. (8)–(11) in Ref. 25] for collisions in a box of 1 cm^3 volume.

Parameter	Ar	He	N_2
SCMFD mean free path	$(1.387\,407 \pm 0.000\,086) \cdot 10^{-2}$	$(3.167\,75 \pm 0.000\,17) \cdot 10^{-2}$	$(3.620\,42 \pm 0.000\,43) \cdot 10^{-2}$
Analytical mean free path	$1.387\,401 \cdot 10^{-2}$	$3.167\,60 \cdot 10^{-2}$	$3.619\,72 \cdot 10^{-2}$
SCMFD mean free time	$(3.647\,46 \pm 0.000\,19) \cdot 10^{-5}$	$(2.635\,23 \pm 0.000\,16) \cdot 10^{-5}$	$(7.968\,14 \pm 0.000\,96) \cdot 10^{-5}$
Analytical mean free time	$3.647\,38 \cdot 10^{-5}$	$2.635\,06 \cdot 10^{-5}$	$7.966\,82 \cdot 10^{-5}$

TABLE III. Comparison of the collision frequency (in $s^{-1}\ m^{-3}$) between the 3D-vt-SCMFD predictions and analytical values for collisions in a box of 1 cm^3 volume, calculated by following the collisions of the trace particles indicated.

Collision type	Analytical	Following Ar	Following He	Following N_2
Ar–Ar	$1.351\,998\,0 \cdot 10^{24}$	$(1.351\,998 \pm 0.000\,069) \cdot 10^{24}$		
Ar–He	$3.769\,823\,0 \cdot 10^{22}$	$(3.767\,1 \pm 0.001\,8) \cdot 10^{22}$	$(3.769\,59 \pm 0.000\,20) \cdot 10^{22}$	
Ar–N_2	$1.243\,945\,8 \cdot 10^{18}$	$(1.10 \pm 0.13) \cdot 10^{18}$		$(1.244 \pm 0.015) \cdot 10^{18}$
He–He	$1.257\,456\,7 \cdot 10^{20}$		$(1.257\,35 \pm 0.000\,76) \cdot 10^{20}$	
He–N_2	$1.125\,945\,8 \cdot 10^{16}$		$(1.080 \pm 0.051) \cdot 10^{16}$	$(1.125\,9 \pm 0.001\,3) \cdot 10^{16}$
N_2–N_2	$1.381\,644\,4 \cdot 10^{11}$			$(1.25 \pm 0.24) \cdot 10^{11}$

We simulate the Poiseuille flow between two parallel plates 0.1 m apart from each other. The y and z directions are periodic, and the walls in the x direction are thermally reflective. The pressure gradient is achieved by accelerating each particle according to $a = -\frac{1}{\rho_m}\frac{\partial p}{\partial z}$, where $\frac{\partial p}{\partial z}$ is the effective pressure gradient and ρ_m is the mass density. It should be noted that there is a distinction between acceleration-driven and pressure-driven flows. The former (as adopted in this work) accelerates the particles, whereas the latter uses boundary conditions to introduce a pressure gradient explicitly. The two flow regimes are closely related; the acceleration term and the pressure gradient are treated in the same way in the Navier–Stokes equation and are, in the hydrodynamic description, equivalent.[30] In particle-based simulations, the pressure-driven flow is more complex to model. As such, we elected to simulate the acceleration-driven flow. Hence, the pressure gradient $\frac{\partial p}{\partial z}$ is an effective (not an actual) pressure gradient. We model the flow of argon gas, with densities ranging from 10^{19} to 10^{21} m^{-3}. All other simulation parameters adopted for the 3D-vt-SCMFD Poiseuille flow are outlined in the supplementary material. The density, temperature, and velocity profiles in the x and y directions can be found in the supplementary material, Sec. S1.B (including a comparison between the SCMFD temperature profiles and literature results for the Poiseuille flow obtained from DSMC). Here, the discussion will focus on the velocity profile in the z direction, along with the viscosity.

In the high-density regime, this type of flow can be described by the Navier–Stokes equations (see the supplementary material, or Ref. 31) from which the viscosity-dependent velocity profile along the flow direction can be determined. The viscosity of the simulated flow is established by fitting the velocity profile from the Navier–Stokes equations (with parameters μ and λ') to the 3D-vt-SCMFD result using the method of least squares. This is then compared to the theoretical viscosity of a gas system, established using Chapman–Enskog theory, which considers the system as a perturbed ideal flow and derives the viscosity from the Boltzmann equation.[32] For a hard-sphere gas, the viscosity is given by[33]

$$\mu = \frac{5}{16 d_{\text{ref}}^2}\sqrt{\frac{m k_B T}{\pi}}, \tag{8}$$

where d_{ref} is the diameter of the hard-sphere particle and m is the mass.

Chapman–Enskog theory is known to accurately predict the viscosity of a system under high-density conditions, where there are frequent collisions between the gas particles. Under low-density conditions, however, the Chapman–Enskog model breaks down as the majority of collisions involve gas particles hitting the walls of the rectangular channel, rather than collisions between gas particles. In addition, the acceleration is inversely proportional to the density—leading to higher perturbations on the flow, which is yet another reason for the breakdown of the theoretical description. Hence, at low densities, the properties of the wall and the acceleration become more important, and the principles of free molecular flow become more applicable.

The velocity profiles (at both low and high densities) for the flow between two plates are shown in Fig. 2, along with the fit to the Navier–Stokes equation [Eq. (S4) in the supplementary material]. The parabolic fit is able to describe the flow profile in the high density system (right), in contrast to the low density regime (left) where the theoretical description is no longer valid.

The viscosity of argon, obtained by fitting the Poiseuille flow profile to the 3D-vt-SCMFD simulations, is plotted alongside the

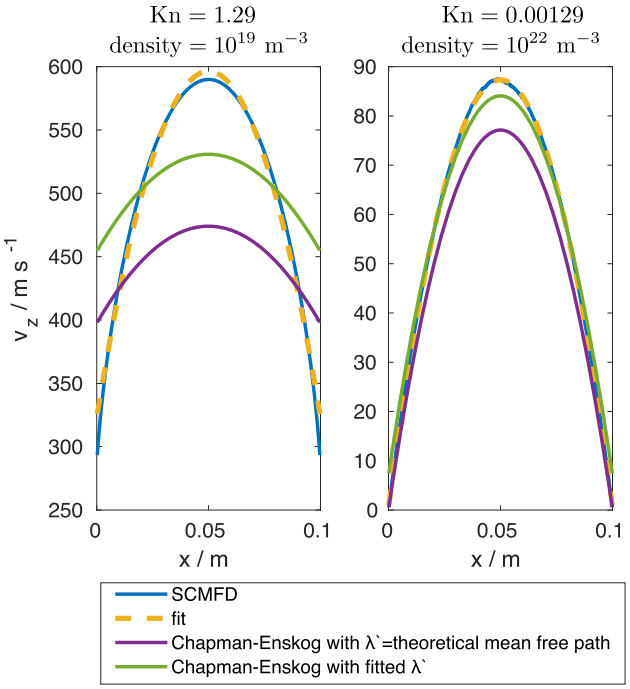

FIG. 2. The stream velocity profile of the one-dimensional Poiseuille flow for high density (10^{22} m^{-3}, right) and low density (10^{19} m^{-3}, left). The SCMFD result (blue) is fitted (dashed yellow) to the solution of the Navier–Stokes equation [Eq. (S4) in the supplementary material] to obtain the viscosity and the parameter λ'. The theoretical velocity profile resulting from the Chapman–Enskog viscosity depends on the slip-condition parameter λ'; it is plotted once with λ' equal to the theoretical mean free path (purple) and once with λ' determined using a non-linear least-squares fit (green). In both cases, the resulting profile is consistently smaller than the result produced by SCMFD (~15% in the high-density case, right).

prediction from Chapman–Enskog theory in Fig. 3. As predicted by Chapman–Enskog [Eq. (8)], the viscosity is constant at low Knudsen numbers, i.e., in the hydrodynamic regime for different slit lengths (L = 0.01–0.1 m). The viscosity is also constant at different pressure gradients ($\frac{\partial p}{\partial z} = -1, -0.5$ N/m^3). The slip length, λ', is determined in the same fitting procedure as the viscosity, as set out in the supplementary material and discussed in Sec. S1.C. The Knudsen number is given by the ratio of the mean free path to the slit size, $\mathrm{K_n} = 1/(d_{\mathrm{ref}}^2 \pi \sqrt{2} \rho L_x)$, and is a measure of how well fluid dynamics can describe the behavior of a system. The simulated 3D-vt-SCMFD viscosity is ~15% lower than the Chapman–Enskog result. The same phenomenon has been identified in the SCMFD simulation of the Couette flow.[25]

To investigate how the 3D-vt-SCMFD viscosity results may depend on the choice of subcell parameters, we quantify the measured viscosity as a function of subcell length to the mean free path ratio in Fig. 4. When the length of a subcell is larger than the mean free path (i.e., when the standard DSMC subcell length guidelines are not followed), the viscosity is overestimated. Such results are expected (and are also detected in DSMC simulations[34]) as the method assumes the same density and velocity distribution everywhere in the subcell: the subcell length determines the length

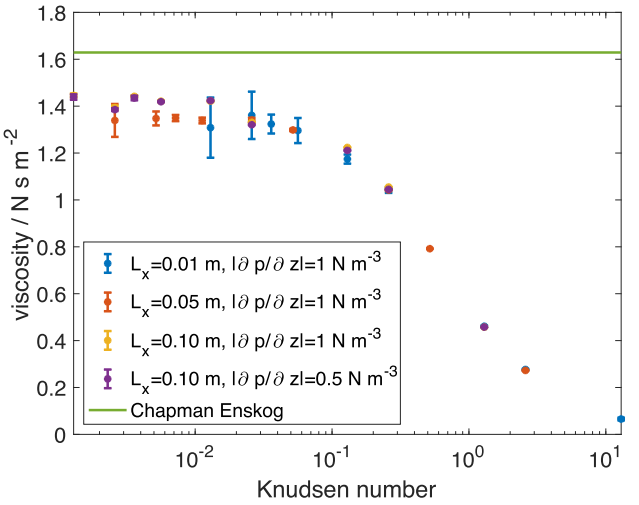

FIG. 3. The viscosity of a Poiseuille flow of Ar gas as established from SCMFD simulations (blue, red, yellow, and purple) and from Chapman–Enskog calculations [green, Eq. (8)] at 273 K, plotted as a function of Knudsen number. The error bars indicate one standard error of the mean. The data are obtained from systems with different slit sizes (L_x = 0.01–0.1 m), with effective pressure gradients ($\frac{\partial p}{\partial z} = -1, -0.5$ N/m^3) driving the flow. The value of the viscosity is determined by fitting Eq. (S4) in the supplementary material to the velocity profile.

over which the properties in the system are constant. In real systems, the mean free path is the length scale over which the properties of the system change. Having subcells larger than the mean free path, thus, enforces correlations over artificially large distances, leading

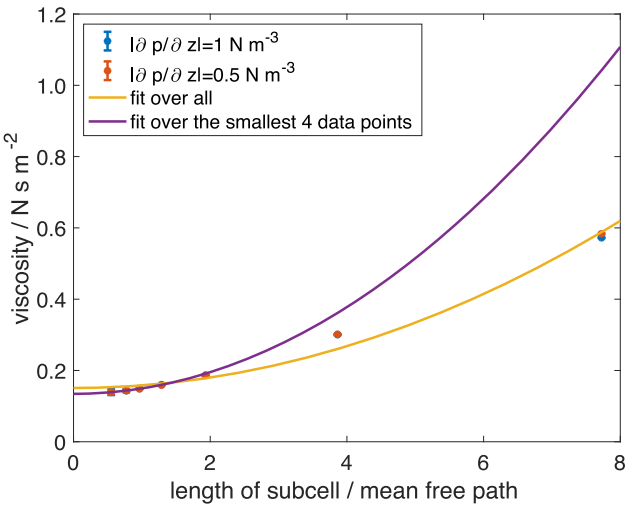

FIG. 4. The convergence of the viscosity as a function of subcell length [divided by the theoretical mean free path, given by Eq. (8) in Ref. 25]. The data are obtained from a simulation with an average density of $5 \cdot 10^{21}$ m^{-3}, but similar features are seen in lower densities as well. The blue and red data are obtained from systems with different pressure gradients [$\frac{\partial p}{\partial z} = -1$(blue), -0.5(red) N/m^3] for the one-dimensional Poiseuille flow by fitting Eq. (S4) in the supplementary material to the velocity profile. The data are fit using the function $\mu(\tilde{x}) = A + B\tilde{x}^2$, both considering all data points (yellow) and when excluding the highest few values (purple; see the main text for further details).

to increased viscosity and, consequently, to a perturbed velocity profile.

Alexander *et al.*[35,36] investigated the dependence of viscosity on the subcell length using Green–Kubo theory, obtaining the relationship

$$\mu = \frac{5}{16 d_{\mathrm{ref}}^2}\sqrt{\frac{m k_B T}{\pi}}\left(1 + \frac{16}{45\pi}\frac{L_x^2}{n_{\mathrm{cell,x}}^2 \lambda^2}\right), \tag{9}$$

where $n_{\mathrm{cell,x}}$ is the number of subcells in the x direction (i.e., between the walls), L_x is the distance between the walls and $\lambda = 1/(\sqrt{2}\pi d_{\mathrm{ref}}^2 \rho)$ is the mean free path. A comparison with Eq. (8) shows that the first factor is equal to the Chapman–Enskog viscosity. The data in Fig. 4 can be fit using the functional form $\mu(\tilde{x}) = A + B\tilde{x}^2$, where $\tilde{x} = \frac{L_x}{n_{\mathrm{cell,x}}\lambda}$. Using all data points in Fig. 4 yields a poor fit. However, when discarding the highest few data points of each simulation set (i.e., considering the first four data points for the simulation with $|\partial p/\partial z| = 1$ N/m^3 and another four data points with

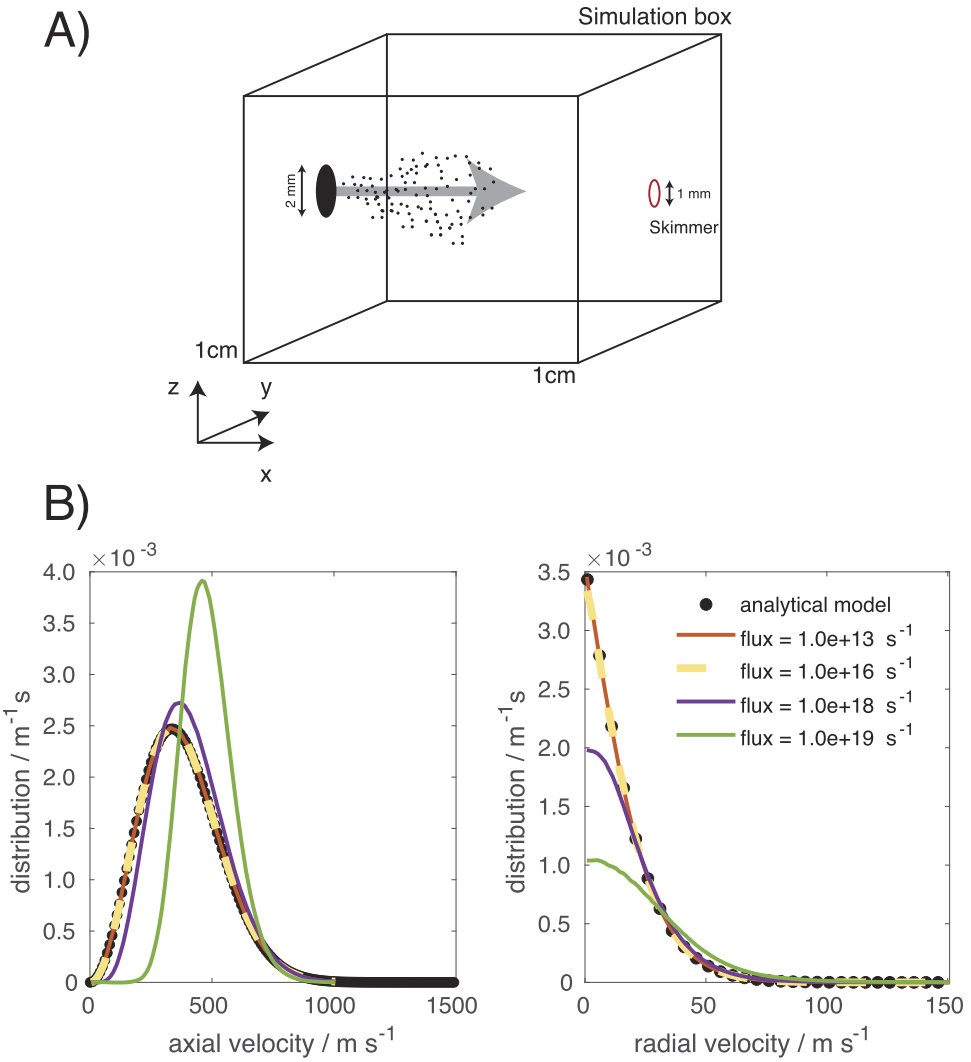

FIG. 5. (a) Schematic depiction of the expansion as modeled in the 3D-vt-SCMFD simulations. Particles are created on an aperture disk (shown in black) and expand into high vacuum. The wall where the aperture is located is thermally reflecting; collisions with all other walls remove the particle from the simulation. The properties of the flow are determined along the beam axis in the x direction and when particles fly through a skimmer (shown in red) located at a distance of 1 cm from the inlet aperture. (b) Velocity distributions of the expanded beams, under different sets of conditions. The velocity distribution is plotted at a distance of 1 cm from the valve, with the particles passing through a virtual skimmer of 0.5 mm radius. (Left) 3D-vt-SCMFD velocity distributions along the beam propagation axis are plotted for four different fluxes, alongside the analytical prediction [black dots, supplementary material, Eq. (S18)]. (Right) Radial velocity distribution is plotted for the same systems. Again, the analytical model [black dots, supplementary material, Eqs. (S19)–(S26)] is in quantitative agreement with the 3D-vt-SCMFD simulations for the two lowest densities considered.

$|\partial p/\partial z| = 0.5$ N/m^3, giving eight data points in total), an excellent fit to the simulation data can be achieved. In the fit to the first eight data points, the parameters are $A = 1.3443 \cdot 10^{-5}$ N s m^{-1}, which is 85.06% of the theoretical Chapman–Enskog viscosity in Eq. (8), and $B = 1.5208 \cdot 10^{-6}$. The dependence on L_x is determined by the factor $B/A = 0.113\,13$, which is very close to the theoretical estimate of $\frac{16}{45\pi} = 0.113\,18$. The squared dependence on the subcell size is derived from the potential contribution to the viscosity[35] and the constant part from the kinetic contribution. The excellent agreement between the theoretical estimate and the value of B/A from the fit parameters demonstrates that the SCMFD method treats the kinetic and potential contribution to the viscosity consistently.

Considering we employ an appropriate choice of subcell size with respect to the mean free path, we cannot give a definite reason for the deviation of the SCMFD viscosity and the theoretical Chapman–Enskog value. It may arise from the way that the mean field is represented in SCMFD: by using a limited number of samples to describe the underlying velocity distribution. Another potential representation could be the use of a Gaussian distribution whose standard deviation (i.e., temperature) depends on the location in the simulation box. Such a representation is sensible in the high-collision regime because it is the first-order correction to the solution of the Boltzmann equation in the Chapman–Enskog theory and has been successfully implemented by Takahashi *et al.*[22] to simulate buffer gas cells. For low-collision regimes, however, this might lead to conflicting results. This is the case, for example, when considering two beams crossing at very low densities. Most of the particles will not experience collisions, and therefore, the system is unlikely to be well described by a single Gaussian distribution; the local velocity distribution would be better represented by two separate Gaussians, centered at the mean velocity of each beam.

C. Expansion

A stringent test of the 3D-vt-SCMFD method is to examine how well it can model the expansion of a gas from a high-pressure reservoir, through a small orifice, and into a low-pressure region. This is directly related to our goal of simulating collisions within a buffer gas cell as such an expansion occurs when particles pass through the exit aperture of the cell. The properties of the beam are highly dependent on the system: low-density conditions give rise to effusive beams, whereas high-density conditions yield a

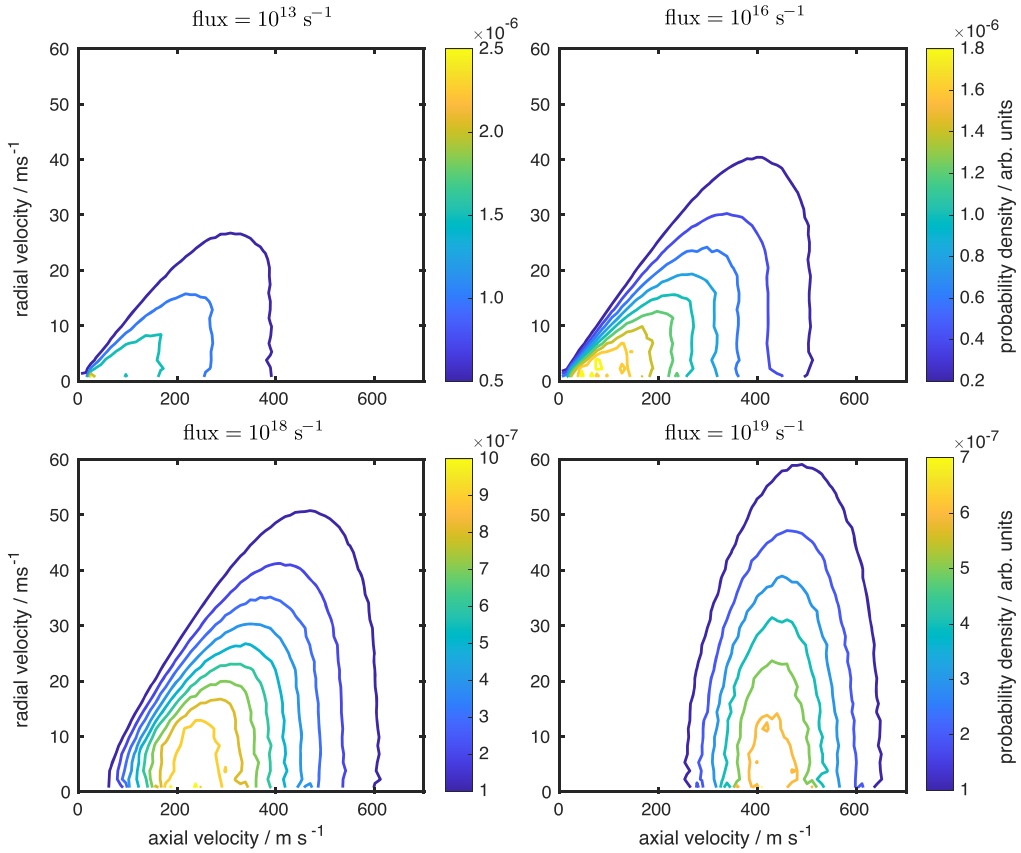

FIG. 6. Plot of the radial and axial velocity distributions, for four different fluxes, recorded at a distance of 1 cm from the source and with a virtual skimmer of 0.5 mm radius in place. Colors indicate relative intensity, from low (blue) to high (yellow).

hydrodynamic expansion. Expansions are commonly used in experiments to generate internally cold molecular beams—with the technique frequently adopted in, for example, high-resolution spectroscopy applications[37,38] and cold chemical reaction studies.[23,24,39,40]

Previous simulations of similar systems include modeling of the micronozzle within a spacecraft thruster system using a DSMC approach,[41] with the Fokker–Planck-DSMC hybrid method also adopted to model the gas flow through a micronozzle[42] (and through a slit[43]). However, neither of these simulations are directly comparable to the conditions described in this work. The strength of the 3D-vt-SCMFD approach is the ability to include the physical features of a system without sacrificing accuracy or making the calculations intractable, and more complex geometries could be implemented straightforwardly.

We perform 3D-vt-SCMFD simulations for a range of gas fluxes, with the expanding gas generated on a disk of radius 1 mm and flying through a skimmer of radius 0.5 mm (1 cm downstream from the source) to replicate the setup commonly adopted in experimental gas expansions. A sketch of the model system can be seen in Fig. 5(a). The simulated system is initially empty (i.e., the mean field has zero density everywhere) and is gradually filled by argon atoms. The particles are generated uniformly on the disk with velocity distributions corresponding to a gas reservoir at 273 K, which is identical to the distribution of a thermal reflective wall.[26] The same distribution was used in Ref. 15, where a similar expansion was investigated using a DSMC method. Once the density, velocity, and temperature of the mean field stabilize, the system is deemed to be in a steady state. To reach steady state conditions typically involves 400 updates of the mean field. Between each update, 200 000 particle trajectories are calculated. The mean field is then used as the starting configuration for the simulated expansion. The resulting data can be analyzed either locally (i.e., on a grid over the whole system, with each grid point corresponding to a subcell) or one can

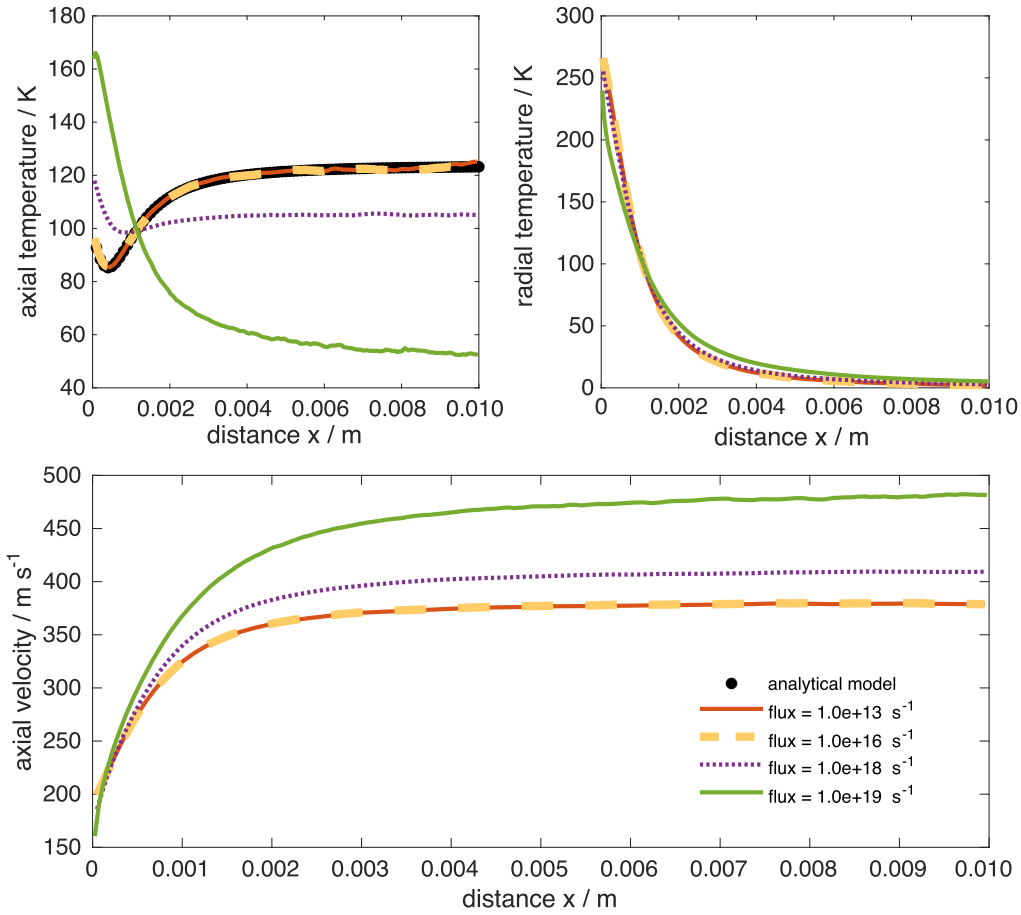

FIG. 7. (Top) Average translational temperature (left: axial temperature, right: radial temperature) of the particles traveling along the beam propagation axis is plotted as a function of distance from the source for four different fluxes. The analytical model [supplementary material, Eqs. (S15)–(S17)] is in excellent agreement with the effusive 3D-vt-SCMFD distributions (lowest two fluxes). (Bottom) Average 3D-vt-SCMFD axial velocity is plotted as a function of distance from the valve for the same four fluxes. In all cases, the particles are accelerated for ~5 mm (corresponding to ~5 valve radii). As expected, the highest flux yields the highest axial velocity; there is little difference in the final velocity of the two lowest-flux beams, which operate in the effusive regime.

focus on particles that successfully fly through the skimmer disk opposite the inlet aperture at a distance of 1 cm. A more detailed description of the simulation parameters is given in the supplementary material.

The velocity distributions of the expanded beams are presented in Figs. 5(b) and 6. The distributions represent the properties of particles that successfully fly through a virtual skimmer. We consider four different fluxes spanning 10^{13}–10^{19} s^{-1} to illustrate the transition from an effusive to a hydrodynamic flow. The two lowest fluxes (corresponding to 10^{13} s^{-1} and 10^{16} s^{-1}) agree quantitatively with the analytical model, which is based on a collision-free environment (see the supplementary material, Sec. S2). For higher fluxes, the axial velocity (also referred to as the beam or forward velocity) of the beam shifts to higher velocities. At the highest flux studied, the significant number of collisions in the beam give rise to a higher axial velocity with a narrower distribution [see Fig. 5(b), left], yielding the behavior expected for supersonic expansions. For low fluxes, 3D-vt-SCMFD reproduces the analytical model [supplementary material, Eq. (S18)] perfectly. The shape of the radial velocity distribution [Fig. 5(b), right] also depends on the flux, with the lowest two fluxes again in excellent quantitative agreement with the analytical model predictions [supplementary material, Eqs. (S19)–(S26)].

The complete two-dimensional velocity distribution of the skimmed beam is shown in Fig. 6. The plots reveal a clear correlation between the radial and axial velocity distributions, with non-symmetrical distributions at lower fluxes. This can be explained geometrically: if the radial velocity is too large compared to the axial velocity, the particle will not be able to fly through the skimmer. Located at a distance of 1 cm from the source and with a radius of 0.5 mm, the skimmer only transmits particles that travel close to the central beam axis. In the low density regime, the skimmer

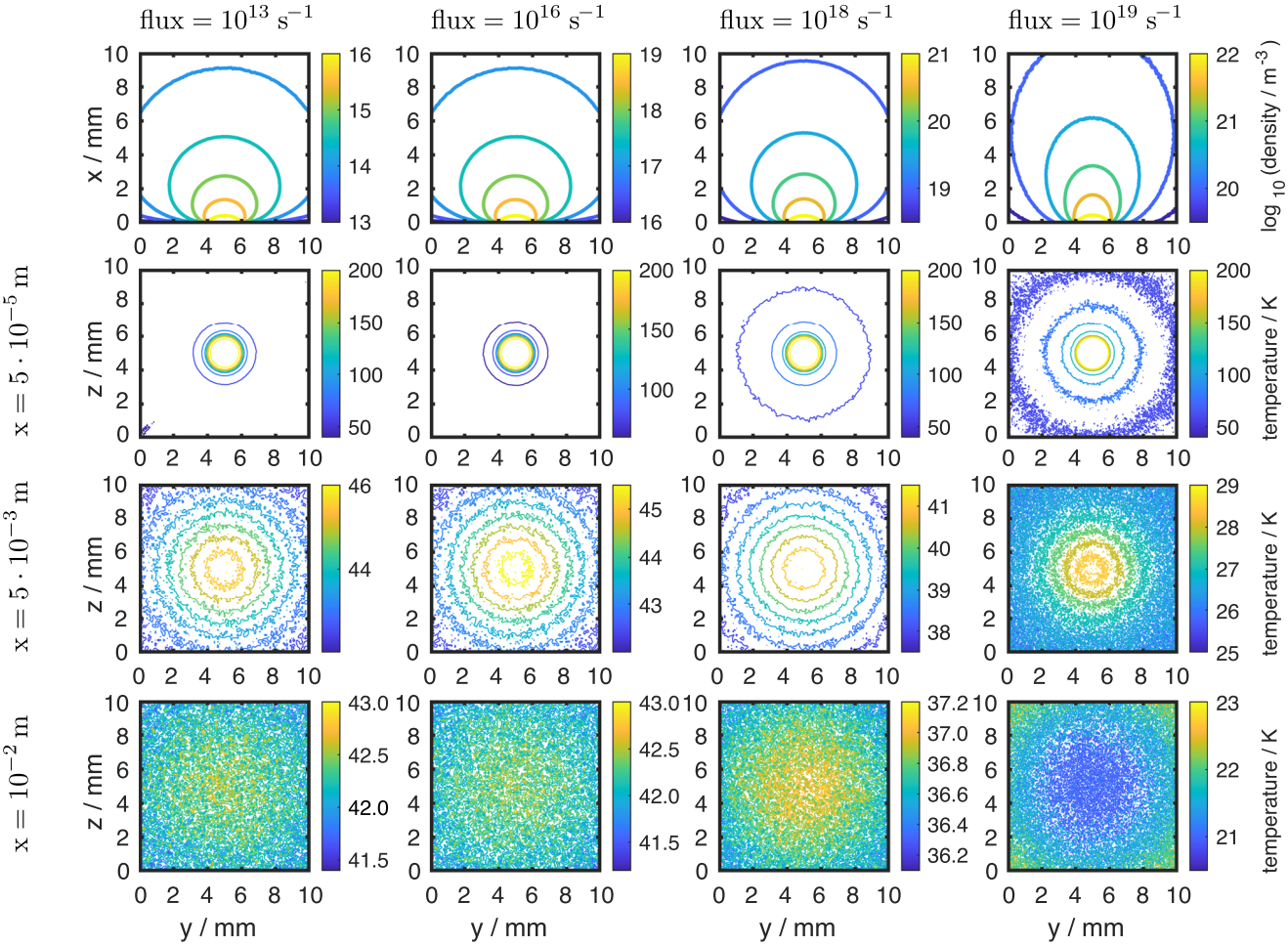

FIG. 8. 3D-vt-SCMFD density (top row) and temperature profiles (second to fourth rows, sampled at three different distances along the *x* axis) of Ar gas expansions are plotted for four different fluxes. The density is plotted along the beam propagation axis; temperature distributions are plotted as cuts through the beam, perpendicular to the propagation axis (i.e., in the *yz* plane, at selected *x* positions). Color bars indicate relative intensity, from low (blue) to high (yellow).

cuts off any velocity with an angle greater than ≈6°. In contrast, the supersonic expansion (bottom right plot) exhibits a more symmetric radial velocity distribution centered around a higher axial velocity. As the particles have a higher axial velocity, they cover the distance to the skimmer much faster, and there is insufficient time for the radical velocity to deflect the trajectory of the particle away from the central beam axis.

Figure 7 depicts the temperature (left: axial temperature, right: radial temperature) and the axial velocity as a function of the distance to the inlet aperture. For low fluxes, where the flow is effusive, the temperature can be estimated quantitatively with the analytical model [see the supplementary material, Eqs. (S15)–(S17)]. The axial temperature initially decreases before increasing to a constant value. The initial drop is a purely geometrical effect, also predicted by the analytical model, and occurs within the first 1–2 inlet radii (≈1–2 mm) of the source. In the hydrodynamic regime, where the beam supersonically expands, the axial temperature decays rapidly and monotonically. In both the effusive and supersonic regimes, the transverse (or radial) temperature decreases as a function of distance. Figure 7 (bottom plot), depicting the average axial velocity as a function of distance from the source, reveals that the majority of the acceleration occurs in the first five valve radii. As expected, the highest flux—corresponding to a supersonic expansion—yields the highest axial velocity. Similar results were obtained simulating the same system using DSMC.[15]

Finally, Fig. 8 shows the density and temperature profiles for different cuts through the expansion. The features of the density distribution (top row) only start to change at higher fluxes, where the narrower axial velocity distribution gives rise to a more focused beam. The average SCMFD temperature plots show further differences between the properties of effusive (two left most columns) and supersonic (right column) expansions: in an effusive flow, the center of the beam exhibits the highest temperature, whereas the temperature distribution inverts after some distance in the supersonic expansion. As the flux of the gas expanding through the orifice is increased, the properties of the resulting beam start to change. These differences can be clearly seen in Figs. 5(b) and 6–8.

The 3D-vt-SCMFD model successfully describes the transition from effusive to hydrodynamic expansions, accurately predicting the behavior expected from beams operating under different regimes. Future work could see 3D-vt-SCMFD applied to related systems with more complexity. One such target is to describe the collisions in a cryogenic buffer gas cell—potentially also accounting for the inelastic collisions that cool the internal molecular degrees of freedom (by including cross sections calculated as a function of energy).[15] Another target system includes describing the collisions that occur in a capillary attached to the face plate of a pulsed valve, where a dissociation laser focused on the capillary can generate photofragments. The collisions that these photofragments undergo and the properties of the gas mixture as it passes through the capillary and expands into a vacuum chamber cannot be precisely simulated with existing models.

IV. CONCLUSION

The 3D-vt-SCMFD model introduced in this work can be applied to a range of different gas-phase environments. The basis of the SCMFD approach is the construction of a mean field to describe the properties of the background gas environment, through which the collisions of particles of interest can be explicitly traced. The properties ascertained from SCMFD simulations are in good agreement with predictions from existing theoretical models, for all systems considered in this work. The largest difference between the values obtained from 3D-vt-SCMFD simulations and from theoretical predictions can be found in the viscosity measurement for the Poiseuille flow. This discrepancy—an offset of ~15% when compared to established theoretical viscosity calculations—has been observed previously[25] and is (tentatively) attributed to the representation of the mean field. For future work, different kernel density estimations could be included to represent the mean field more accurately. Additionally, generating the background gas environment with experimental results (as done in Refs. 23 and 24) or other simulation algorithms (as seen in Ref. 22) could be considered. However, such external mean fields are only suitable if the background gas environment is not influenced by the new species that travels through it. On the other hand, such representations might open up the possibility of investigating time-dependent processes—something that 3D-vt-SCMFD is currently not able to do, but that would be an extremely useful extension of the method.

In summary, this work demonstrates that the 3D-vt-SCMFD algorithm is robust, versatile, accurate, and efficient. The method successfully describes different gas expansions and trace components in a gas mixture and is, therefore, ideally suited to modeling collisions in environments such as a buffer gas cell. Beyond the modeling of buffer gas cells, this work demonstrates that the 3D-vt-SCMFD method can be readily applied to a wide range of different collision environments.

SUPPLEMENTARY MATERIAL

See the supplementary material for Poiseuille flow (S1), analytic description of expansion (S2): free molecular flow limit, and SCMFD simulation input parameters (S3).

ACKNOWLEDGMENTS

B.R.H. acknowledges funding provided by the EPSRC (Project No. EP/N032950/2) and the ERC (Starting Grant Project No. 948373).

AUTHOR DECLARATIONS

Conflict of Interest

The authors have no conflicts to disclose.

DATA AVAILABILITY

The 3D-variable time step SCMFD code is freely available at Ref. 44. The data that support the findings of this study are available within the article and its supplementary material.

REFERENCES

[1] G. A. Bird, *Molecular Gas Dynamics and the Direct Simulation of Gas Flows* (Clarendon Press, Oxford, 1994).
[2] G. A. Bird, Phys. Fluids **6**, 1518 (1963).

[3]P. J. Hoogerbrugge and J. M. V. A. Koelman, Europhys. Lett. **19**, 155 (1992).
[4]R. D. Groot and P. B. Warren, J. Chem. Phys. **107**, 4423 (1997).
[5]U. Frisch, B. Hasslacher, and Y. Pomeau, Phys. Rev. Lett. **56**, 1505 (1986).
[6]S. Chen and G. D. Doolen, Annu. Rev. Fluid Mech. **30**, 329 (1998).
[7]A. Malevanets and R. Kapral, J. Chem. Phys. **110**, 8605 (1999).
[8]G. Gompper, T. Ihle, D. M. Kroll, and R. G. Winkler, *Advanced Computer Simulation Approaches for Soft Matter Sciences III*, Advances in Polymer Science Vol. 221 (Springer, Berlin, 2008), p. 1.
[9]K. S. Twyman, M. T. Bell, B. R. Heazlewood, and T. P. Softley, J. Chem. Phys. **141**, 024308 (2014).
[10]S. Hofsäss, M. Doppelbauer, S. C. Wright, S. Kray, B. G. Sartakov, J. Pérez-Ríos, G. Meijer, and S. Truppe, New J. Phys. **23**, 075001 (2021).
[11]A. Amirav, U. Even, and J. Jortner, Chem. Phys. **51**, 31 (1980).
[12]S. M. George, Chem. Rev. **110**, 111 (2010).
[13]N. R. Hutzler, H.-I. Lu, and J. M. Doyle, Chem. Rev. **112**, 4803 (2012).
[14]B. R. Heazlewood and T. P. Softley, Nat. Rev. Chem. **5**, 125–140 (2021).
[15]O. Schullian, J. Loreau, N. Vaeck, A. van der Avoird, B. R. Heazlewood, C. J. Rennick, and T. P. Softley, Mol. Phys. **113**, 3972 (2015).
[16]M. J. Doppelbauer, O. Schullian, J. Loreau, N. Vaeck, A. van der Avoird, C. J. Rennick, T. P. Softley, and B. R. Heazlewood, J. Chem. Phys. **146**, 044302 (2017).
[17]E. S. Oran, C. K. Oh, and B. Z. Cybyk, Annu. Rev. Fluid Mech. **30**, 403–441 (1998).
[18]G. J. LeBeau and F. E. Lumpkin III, Comput. Methods Appl. Mech. Eng. **191**, 595–609 (2001).
[19]G. Di Staso, H. J. H. Clercx, S. Succi, and F. Toschi, Philos. Trans. R. Soc., A **374**, 20160226 (2016).
[20]I. D. Boyd, J. Thermophys. Heat Transfer **10**, 579–585 (1996).
[21]S. Rjasanow and W. Wagner, J. Comput. Phys. **124**, 243–253 (1996).
[22]Y. Takahashi, D. Shlivko, G. Woolls, and N. R. Hutzler, Phys. Rev. Res. **3**, 023018 (2021).
[23]P. Allmendinger, J. Deiglmayr, O. Schullian, K. Höveler, J. A. Agner, H. Schmutz, and F. Merkt, ChemPhysChem **17**, 3596 (2016).
[24]P. Allmendinger, J. Deiglmayr, K. Höveler, O. Schullian, and F. Merkt, J. Chem. Phys. **145**, 244316 (2016).
[25]O. Schullian and B. R. Heazlewood, Mol. Phys. **117**, 3076 (2019).
[26]F. J. Alexander and A. L. Garcia, Comput. Phys. **11**, 588 (1997).
[27]K. Nanbu, J. Phys. Soc. Jpn. **49**, 2042–2049 (1980).
[28]C. Greengard and L. G. Reyna, Phys. Fluids A **4**, 849 (1992).
[29]G. A. Bird, Prog. Astronaut. Aeronaut. **118**, 211–226 (1989); available at https://ui.adsabs.harvard.edu/abs/1989PrAA..117..211B/abstract.
[30]Y. Zheng, A. L. Garcia, and B. J. Alder, J. Stat. Phys. **109**, 495 (2002).
[31]C. Pozrikidis, *Fluid Dynamics* (Springer Science+Business Media, New York, 2001).
[32]S. Chapman and T. G. Cowling, *The Mathematical Theory of Non-Uniform Gases: An Account of the Kinetic Theory of Viscosity, Thermal Conduction and Diffusion in Gases*, 3rd ed. (Cambridge University Press, Cambridge, 1970).
[33]H. Sigurgeirsson and D. M. Heyes, Mol. Phys. **101**, 469 (2003).
[34]Z.-X. Sun, Z. Tang, Y.-L. He, and W.-Q. Tao, Comput. Fluids **50**, 1 (2011).
[35]F. J. Alexander, A. L. Garcia, and B. J. Alder, Phys. Fluids **10**, 1540 (1998).
[36]F. J. Alexander, A. L. Garcia, and B. J. Alder, Phys. Fluids **12**, 731 (2000).
[37]L. Semeria, P. Jansen, G.-M. Camenisch, F. Mellini, H. Schmutz, and F. Merkt, Phys. Rev. Lett. **124**, 213001 (2020).
[38]G. Clausen, P. Jansen, S. Scheidegger, J. A. Agner, H. Schmutz, and F. Merkt, Phys. Rev. Lett. **127**, 093001 (2021).
[39]J. Toscano, H. J. Lewandowski, and B. R. Heazlewood, Phys. Chem. Chem. Phys. **22**, 9180–9194 (2020).
[40]L. Y. Wu, C. Miossec, and B. R. Heazlewood Phys. Chem. Comm. **58**, 3240–3254 (2022).
[41]Z. Yang and Y. Hai Wei, Aircr. Eng. Aerosp. Technol. **78**(5), 387 (2006).
[42]S. Küchlin and P. Jenny, J. Comput. Phys. **363**, 140 (2018).
[43]E. Jun, M. Grabe, and K. Hannemann, AIP Conf. Proc. **2132**, 070001 (2019).
[44]O. Schullian, H. S. Antila, and B. R. Heazlewood (2021). "3D-vt-SCMFD code," Zenodo. https://doi.org/10.5281/zenodo.5779389